INSTITUT DE FRANCE
Académie des sciences

Comptes Rendus
Mécanique

Ali Hadj and Mohammed Boulenouar

CFD analysis of operating condition effects on optimum nozzle exit position of a supersonic ejector using the refrigerant R134a

Volume 349, issue 1 (2021), p. 189-202.

<https://doi.org/10.5802/crmeca.60>

© Académie des sciences, Paris and the authors, 2021.
Some rights reserved.

This article is licensed under the
Creative Commons Attribution 4.0 International License.
http://creativecommons.org/licenses/by/4.0/

Les Comptes Rendus. Mécanique *sont membres du Centre Mersenne pour l'édition scientifique ouverte*
www.centre-mersenne.org

Comptes Rendus
Mécanique
2021, 349, nº 1, p. 189-202
https://doi.org/10.5802/crmeca.60

Short Paper / *Note*

CFD analysis of operating condition effects on optimum nozzle exit position of a supersonic ejector using the refrigerant R134a

Ali Hadj [a] **and Mohammed Boulenouar** [*, a]

[a] Laboratoire des Sciences et Ingénierie Maritime (LSIM), Department of Maritime Engineering, Faculty of Mechanical Engineering, El Mnaouar, BP 1505, Bir El Djir 31000, USTO Oran, Algeria

E-mails: ali.hadj@univ-usto.dz (A. Hadj), boulenouar_m@yahoo.fr (M. Boulenouar)

Abstract. In this work, the computational fluid dynamics technique is employed to study operating condition effects on the optimum value of an important parameter called the nozzle exit position (NXP) for an ejector design. This ejector uses the gas R134a as the working fluid. Numerical tests are carried out using a combination of the REFPROP 7.0 database state equation and the high-Reynolds version of the SST k–ω model. Good agreement in terms of entrainment ratio and critical temperature is obtained between computed values and measurements. In addition, numerical results indicate that the optimum NXP maximizes ejector performance and is highly dependent on operating conditions.

Keywords. Optimum NXP, Operating conditions, R134a, Entrainment ratio, Refrigeration.

Manuscript received 21st September 2020, revised 3rd November 2020, accepted 17th November 2020.

1. Introduction

The ejector has been widely employed in refrigeration, air conditioning, petroleum refining, desalination, chemical systems, and other fields as an energy-recovering device owing to its simple structure, safety, reliability, and low-grade energy for use as a power source [1]. It is composed of four main parts: a nozzle, a suction chamber, a mixing chamber, and a diffuser. This is schematically shown in Figure 1. Its operating principle is described as follows. A high-velocity flow occurs when high pressure flows through the nozzle throat, and a low-pressure region is formed at the primary nozzle outlet. Therefore, a secondary low-pressure fluid flow is sucked. Moreover, energy exchange due to the turbulent diffusion phenomenon between the high pressure and the sucked surrounding flows generates a mixing fluid of intermediate pressure. After the flow enters the

* Corresponding author.

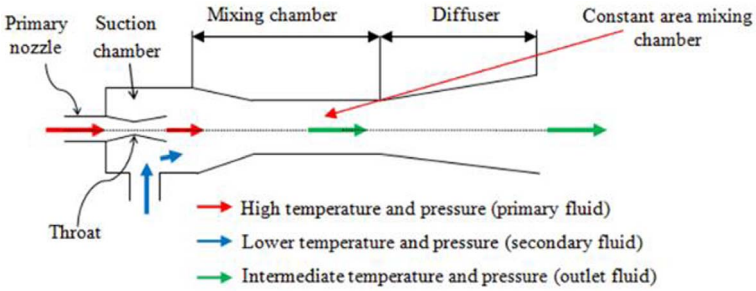

Figure 1. Schematic view of a supersonic ejector.

mixing chamber, flow velocities tend to equalize and the mixed flow is pressurized. Subsequently, the mixture flows to the diffuser and its velocity falls gradually so that kinetic energy is converted into potential energy and a relatively high-pressure flow occurs [2].

Several factors such as the compression ratio R_{COM} are used to assess the performance of an ejector refrigeration system. This factor is the static pressure at the exit of the diffuser P_{DIF} divided by the static pressure of the evaporator inlet P_{EV}:

$$R_{\mathrm{COM}} = \frac{P_{\mathrm{DIF}}}{P_{\mathrm{EV}}}. \tag{1}$$

The coefficient of performance COP is expressed as follows:

$$\mathrm{COP} = \frac{Q_{\mathrm{EV}}}{Q_{\mathrm{BO}} + W_{\mathrm{P}}} = \frac{\dot{m}_{\mathrm{S}}}{\dot{m}_{\mathrm{P}}} \frac{\Delta h_{\mathrm{EV}}}{\Delta h_{\mathrm{BO}}}. \tag{2}$$

It is defined as the ratio between the evaporation heat energy Q_{EV} (refrigeration effect) and the total incoming energy (boiler and pump) in the cycle.

The entrainment ratio ER is written as follows:

$$\mathrm{ER} = \frac{\dot{m}_{\mathrm{S}}}{\dot{m}_{\mathrm{P}}}. \tag{3}$$

It is defined as the ratio between the secondary and primary mass flow rates $\dot{m}_{\mathrm{S}}$ and $\dot{m}_{\mathrm{P}}$, respectively.

Unfortunately, the performance of the ejector system is still extremely lower than any steam compressor and heat-driven absorption system. This inferior performance is due to the high dependence of the ejector performance on operating conditions, design dimensions, and working fluids [3]. The design dimensions include the distance between the primary nozzle exit and the entrance of the mixing chamber, which is also called the nozzle exit position (NXP). This distance is sometimes presented in its nondimensional form with respect to the throat diameter. This factor has a highly significant effect on the ejector efficiency when the operating conditions are different from the on-design conditions [4–7]. The existence of at least an optimum NXP that maximizes the ejector performance was stated in different studies (Table 1). This table highlights the fact that the effects of operating conditions on ejector performance are relatively well established, but their effects on optimum NXP are less known. In addition, there is no consensus among all these studies about the range of the optimum NXP. Moreover, they are in contrast with the recommendations of the design guide ESDU [8], which suggests that the nozzle should be placed at a distance of 0.5 to 1.0 length of the mixing chamber's throat diameter upstream of the mixing chamber inlet. Therefore, more efforts are required to clarify this issue.

In this study, a computational fluid dynamics (CFD) investigation method for the performance of a single-phase ejector operated with R134a is reported (Table 2). The numerical model is first calibrated by comparing the simulation values to the experimental results obtained from an

Table 1. Value or range of the optimum NXP established in the literature

Reference	Value or range	(Primary)–(secondary)–(discharge) (bar)	Refrigerant
[9]	0.21 (-)	(1.80)–(0.07)–(0.1)	Methanol
[10]	−5 mm	(19.21)–(1.02)–(3.06)	R245fa
[11]	1.7–3.4 (-)	(4.5–6)–(0.435–0.47)–(0.8)	R141b
[12]	8.25, 8.91, 9.57 mm	(20.24–23.13)–(3.94–4.36)–(4.5–4.87)	R134a
[13]	−5 mm	(3.7)–(0.9–1.1)–(1.2)	R134a
[14]	5 mm	(7.3–12.2)–(1.2, 2.88)–(3.2)	R600a
[15]	56–96 mm	(2.7–1.99)–(0.012–0.017)–(0.02)	Steam water
[16]	0	(5.7)–(0.7)–(1.1)	Air
[17]	5–10 mm	(13.44)–(2.21)–(3.91)	R600a
[18]	24.7 mm	(2)–(0.01)–(0.03)	Steam water

Table 2. Thermodynamic properties of the refrigerant R134a

Name	Chemical formula	Molecular weight (kg/kmol)	Critical temperature (°C)	Critical pressure (MPa)	Critical density (kg/m^3)	NBP (°C)	Wet/dry	ODP: Ozone Depletion Potential	GWP: Global Warming Potential	Safety group
R134a	CH_2FCF_3	102.03	101.1	4.06	507.87	−26.50	Wet	0	1300	A1

NBP, normal boiling point.

ejector implemented on an experimental refrigeration cycle [19]. Then, the influence of operating conditions on the optimum NXP is studied. In subsequent sections, a discussion about the CFD model basis and computed results is presented.

2. Numerical modelling

2.1. *Governing equations*

These governing equations are discretized in an axisymmetric domain, where the fluid is assumed compressible and steady and whose walls are smooth and adiabatic.

The continuity equation is expressed as follows:

$$\frac{\partial \rho}{\partial t} + \frac{\partial(\rho u_i)}{\partial x_i} = 0. \tag{4}$$

The momentum equation is expressed as follows:

$$\frac{\partial(\rho u_i)}{\partial t} + \frac{\partial(\rho u_i u_j)}{\partial x_j} = -\frac{\partial P}{\partial x_i} + \frac{\partial \tau_{ij}}{\partial x_j}. \tag{5}$$

The energy equation is written as follows:

$$\frac{\partial}{\partial t}(\rho E) + \frac{\partial u_i(\rho E + P)}{\partial x_i} = \frac{\partial}{\partial x_i}\left(k_{\text{eff}}\frac{\partial T}{\partial x_i}\right) + \frac{\partial}{\partial x_i}(u_j \tau_{ij}). \tag{6}$$

The term τ_{ij} of (5) and (6) can be written in the form

$$\tau_{ij} = \mu_{\text{eff}}\left(\frac{\partial u_i}{\partial x_j} + \frac{\partial u_j}{\partial x_i} - \frac{2}{3}\frac{\partial u_k}{\partial x_k}\delta_{ij}\right). \tag{7}$$

Table 3. Main geometrical parameters of the tested ejector

Parameters	Values
Diameter of nozzle throat (mm)	2.0
Diameter of nozzle exit (mm)	3.0
Angle of nozzle divergence (°)	1.4
Diameter of constant mixing chamber D_{throat} (mm)	4.8
Length of diffuser (mm)	120.15
Length of mixing chamber (mm)	41.39
Length of constant mixing chamber (mm)	21.82
Diameter of diffuser exit (mm)	20
Angle of mixing chamber convergence (°)	30
Nozzle exit position (NXP, mm)	−1.46, −2.8, −14.14, −5.58, −6.82, −8.22, −9.5, −10.85, −12.19, −13.53, 14.87

Table 4a. Experimental operating conditions

	C1		C2		C3	
	T (°C)	P (Pa)	T (°C)	P (Pa)	T (°C)	P (Pa)
Primary	79.37	2,598,000	84.39	2,888,800	89.15	3,188,100
Secondary	10	414,610	10	414,610	10	414,610
ER (EXP)	0.494		0.398		0.339	
T_{CR} (°C) (EXP)	29.41		32.48		35.41	
Superheating temperature: +10 °C						

2.2. *Turbulence model*

The SST k–ω model has been widely used due to its good prediction capabilities for a wide range of turbulent flows such as transonic and adverse pressure gradient flows. This model uses the k–ω wall region and the standard k–ε formulations in the near and the far field, respectively. This model is recommended by different studies and a guide [20–22] since it provides accurate data compared with other models such as k–ω, standard k–ε, realizable k–ε, and k–ε RNG. In this paper, all simulations are performed using this model in the high-Reynolds number range to provide accurate and predicted results in a reasonable running time.

2.3. *Geometrical and numerical conditions*

The main geometrical parameters of the tested supersonic ejector are presented in Table 3 as defined in [19]. All grids are modelled using the software GAMBIT based on two-dimensional and axisymmetric conditions. These conditions are certainly crucial to our purpose since three-dimensional effects do not perturb the accuracy of numerical results as verified by Sharifi and Boroomand [23].

Seven experimental operating conditions are used in this study and are summarized in Tables 4a and 4b. Each condition is denoted as a saturation property (temperature or pressure). The total pressure and temperature are assumed to be nearly equal to their static values (kinetic energies are negligible).

Primary and secondary flow inlets are set as pressure inlets and the outlet flow is set as the pressure outlet. The implicit pressure-based coupled algorithm is adopted to solve the nonlinear governing equations due to high Mach numbers in the flow domain [22]. Convective and diffusion terms are discretized following second-order upwind and central difference schemes, respectively. Table 5 displays the details of the numerical conditions used in this CFD model.

Table 4b. Experimental operating conditions

	C4		C5		C6		C7	
	T (°C)	P (Pa)	T (°C)	P (Pa)	T (°C)	P (Pa)	T (°C)	P (Pa)
Primary	79.37	2,598,000	84.39	2,888,800	89.15	3,188,100	89.15	3,188,100
Secondary	7	374,630	7	374,630	7	374,630	5	349,660
ER (EXP)	0.422		0.342		0.297		0.273	
T_{CR} (°C) (EXP)	28.95		31.68		34.11		32.02	
Superheating temperature: +10 °C								

Table 5. Specific settings introduced in the CFD model

Formulation	Implicit
Solver	Coupled pressure-based
Primary flow	Pressure inlet
Secondary flow	Pressure inlet
Outlet flow	Pressure outlet
Turbulence model	SST k–ω in high-Reynolds number ($30 < y^+ < 60$)
Near-wall treatment	Integrated in the turbulence model
Pressure interpolation	PREssure STaggering Option (PRESTO!)
Gradients and derivative	Least-squares cell-based
Working fluid	R134a

The turbulence intensity I and hydraulic diameters D_H are specified at the inlet and outlet turbulence boundary conditions where kinetic energies are negligible. Numerical studies [22, 24, 25] have indicated that the value 5% is a good estimate for the turbulence intensity in the absence of experimental data. To avoid the divergence of calculations, under-relaxation factors are adjusted at the start from the value 0.5. Convergence is achieved when residues of each equation are not greater than 10^{-6} and are stable.

2.4. *Working fluid*

The tested ejector uses 1,1,1,2-tetrafluoroethane ($C_2H_2F_4$), which is also known as R134a or HFC 134a refrigerant. It is classified as AHSRAE safety group A1 (nonflammable and not toxic). In the present study, this refrigerant is assumed to exist constantly in a single phase since its boiling point is −26.50 °C. The state equation from the Reference Fluid Thermodynamic and Transport Properties (REFPROP) 7.0 equation database is used to calculate the fluid density ρ as a function of thermodynamic variables pressure (P) and temperature (T). This thermodynamic model is based on numerical formulations and experimental measurements of the working fluid R134a available in [26]. However, this numerical model remains stable only at temperatures in the range 170–455 K and pressures up to 70 MPa. Table 6 lists all thermophysical properties used in the CFD model. These properties are assumed to be constant at the average temperature between the secondary inlet and outlet conditions. They were provided by the REFPROP database of National Institute of Standards and Technology (NIST).

3. Details of mesh study

Grid independence is verified by comparing five structured grids. All meshes are refined near walls and also in the vicinity of the mixing layer as shown in Figure 2. In addition, each mesh is

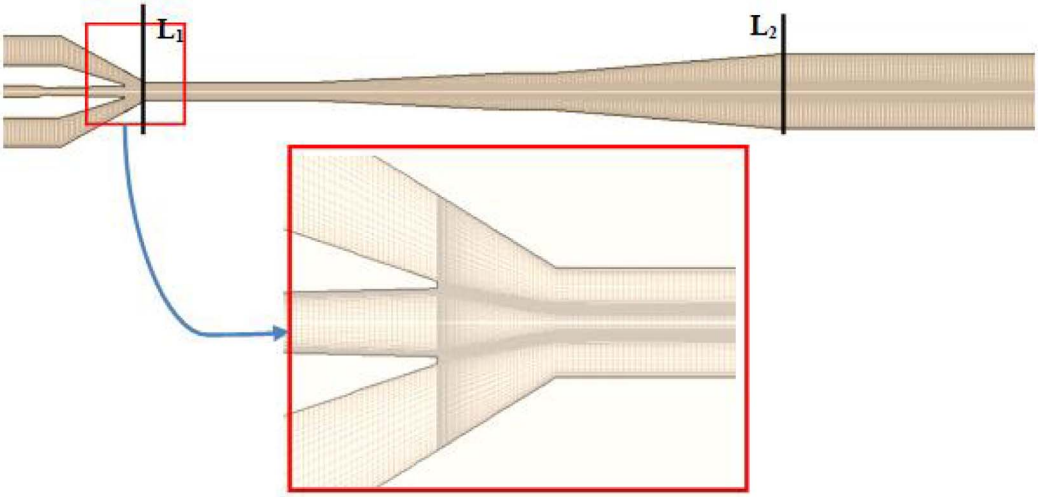

Figure 2. Grid elements of the ejector CFD model.

Table 6. Thermophysical properties of the tested refrigerant used in simulations

Kinematic viscosity $\times 10^{-5}$ (Pa·s)	1.44
Thermal conductivity (W/m/K)	0.021
Heat capacity (J/kg/K)	2240.1

Table 7. Grid independence tests (areas L_1 and L_2; NXP = −5.85 mm)

Mesh	ER	Er (%)	P_{L1} (Pa)	Er (%)	V_{L1} (m/s)	Er (%)	P_{L2} (Pa)	Er (%)	V_{L2} (m/s)	Er (%)
21,930	0.542	—	374,940	—	324.97	—	705,850	—	8.91	—
39,191	0.548	1.09	369,110	1.58	326.55	0.48	705,860	0.00	8.81	1.22
68,161	0.552	0.72	36,5170	1.08	327.30	0.23	705,860	0.00	8.75	0.69
116,075	0.555	0.54	363,030	0.59	327.76	0.14	705,860	0.00	8.71	0.43
207,323	0.556	0.18	361,110	0.53	328.15	0.12	705,860	0.00	8.68	0.32

$$Er\% = \left|\frac{\mathrm{CFD}_{i+1} - \mathrm{CFD}_i}{\mathrm{CFD}_{i+1}}\right| \times 100 \ (i = 5)$$

obtained by increasing the cell number of the previous grid by 33% in all directions as suggested by Çengel and Cimbala [27]. There is approximately a ratio of 1.7 between each of the two successive grids. Table 7 presents the values of entrainment ratios (ER), area-weighted average pressures (P_{L1}), and velocities (V_{L1}) for five grids in two areas L_1 and L_2. It is shown that the entrainment ratios, pressures, and velocities decrease as the number of cells increases. Then they gradually decrease and become negligible especially when the grids contain 116,075 and 207,323 cells, respectively. Figure 3 shows the variation in the Mach number along the ejector axis. Small discrepancies are visible in the region proximal to the diffuser between grids containing 116,075 and 207,323 cells. As regards the real gas model from NIST, it is expected that the solution converges in a longer time than does the ideal gas model due to the complexity of the equations. Moreover, after analysing the numerical tests listed in Table 7, the grid of 116,075 cells is selected for subsequent simulations ($y^+ \approx 50$).

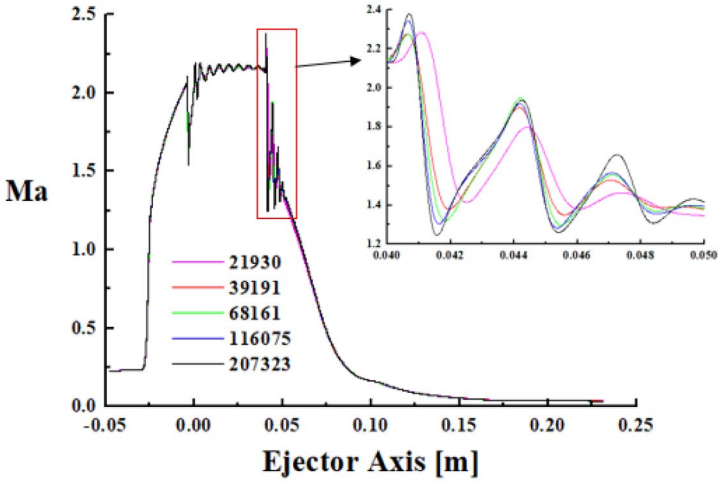

Figure 3. Effects of grid levels on Mach number distribution along the ejector axis for C1 (NXP = −5.85 mm).

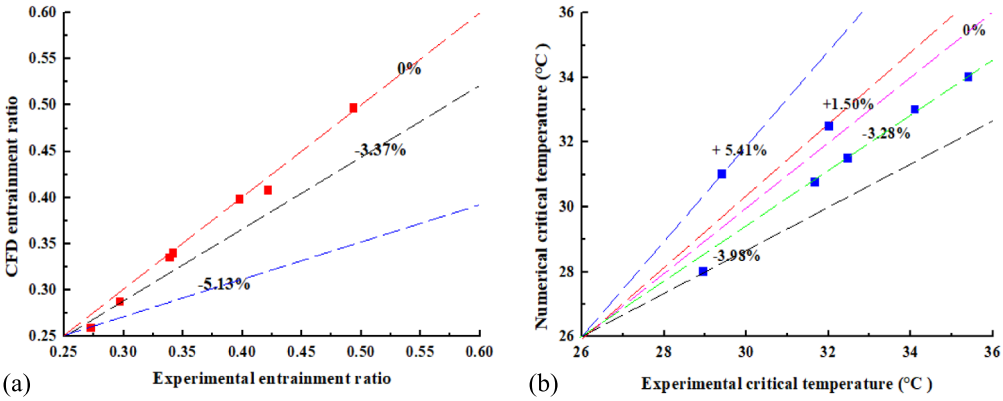

Figure 4. Comparison between numerical and experimental results: (a) entrainment ratio and (b) critical temperature.

4. Results and discussion

4.1. *Validation*

Figures 4(a,b) show plots of computed and experimental values of the entrainment ratio and the critical temperature, respectively, for seven operating conditions (listed in Tables 4a and 4b). Good agreement is noted between these results since the maximum errors are 5.13% and 5.41% for the entrainment ratio and the critical temperature, respectively. Therefore, these findings confirm that the tested numerical model is well adapted to supersonic flows in ejectors.

Figure 5 illustrates the effects of discharge or condenser temperature (T_{DIS}) on predicted and experimental entrainment ratios for C2. The curves contain a similar horizontal part (AB) called the critical mode (on-design condition), which is followed by a sharply decreasing part (BC) called the subcritical mode (off-design condition) [28]. The dividing point of the two parts corresponds to the maximum discharge temperature T_{CR} (point B), which is called the critical temperature. This is commonly considered the operating condition limit, where the ejector is

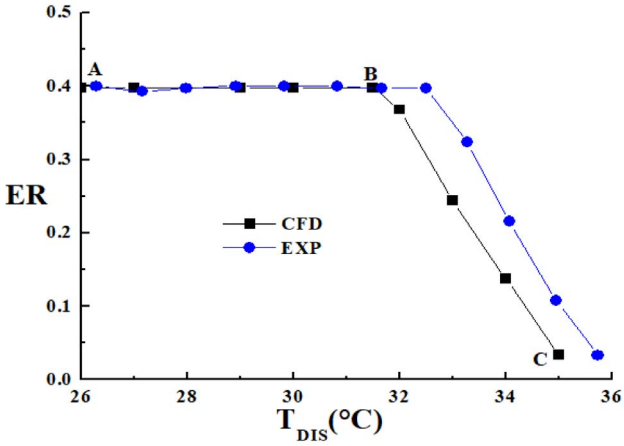

Figure 5. Comparison between entrainment ratio distributions along the ejector axis for C2 (NXP = −5.85 mm).

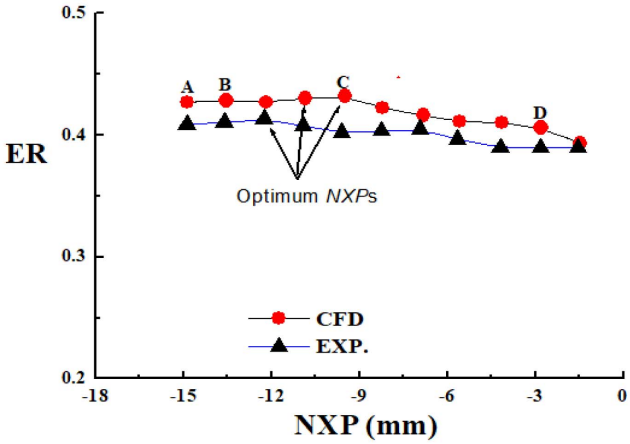

Figure 6. CFD and experimental distributions of entrainment ratio with different NXPs for C2.

at its most efficient working condition. The numerical value T_{CR} = 31.5 °C differs from the experimental value 32.48 °C with a negligible relative error of 3.00%. Good overall agreement is also noted between the numerical results and the experimental data in the on-design and off-design conditions.

The NXP is considered one of the most important geometrical parameters of the ejector [29]. Figure 6 illustrates the comparison between computed and experimental entrainment ratios with different NXPs (listed in Table 3) for condition C2. The experimental and numerical optimum NXPs are at a distance of approximately 2.5 mm from each other. Furthermore, it is noted that the NXP value −5.58 mm selected by [19] does not correspond to the optimum value and may be considered as arbitrary data. Figure 7 depicts the velocity streamlines for different NXPs at the points A, B, C, and D (see Figure 6) for the operating condition C2. It is noted that the expansion of the jet, issuing from the primary nozzle exit, decreases when the NXP increases. Therefore, the pressures of the secondary and primary flows are gradually reduced on the mixing chamber wall, resulting in the disappearance of vortices and an increase in the entrainment ratio up to

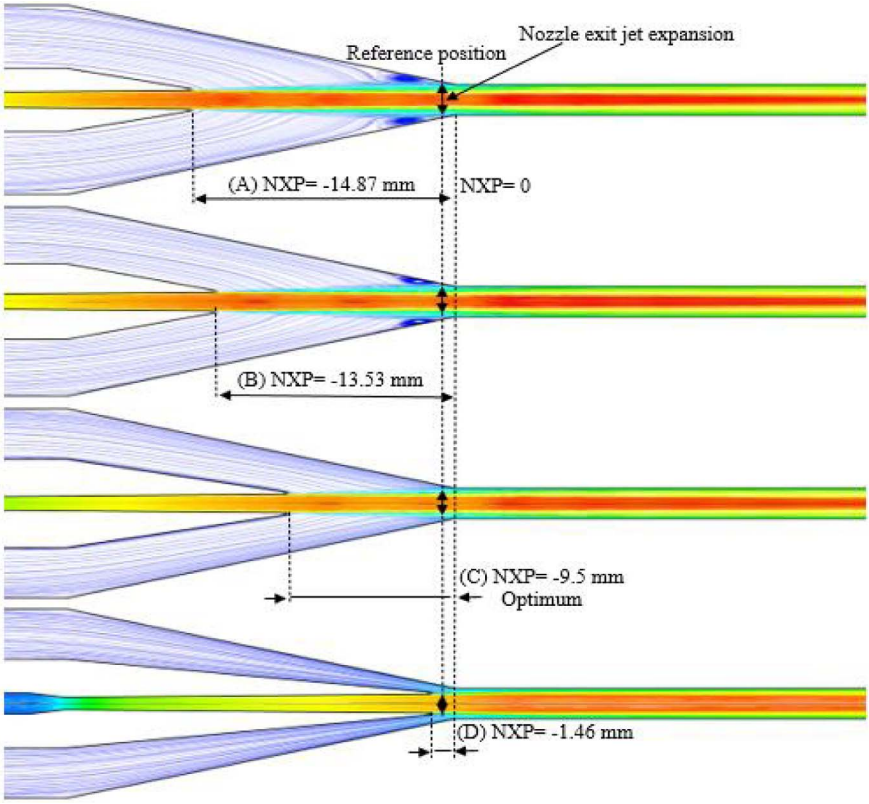

Figure 7. The velocity streamlines at different NXPs for C2.

NXP = −9.5 mm. Then, the excessive speed reduces the ejector performance as the primary nozzle exit moves to the constant mixing chamber's inlet as shown in Figure 6.

4.2. *Effects of operating conditions on the optimum NXP*

4.2.1. *Primary temperature*

Figure 8 displays the distributions of entrainment ratios at critical temperatures for three primary temperatures (79.37, 84.39, and 89.15 °C), which represent conditions C1, C2, and C3, respectively. The secondary temperature is kept constant at 10 °C (Table 4a). It is reported that the increase in the primary temperature produces two effects: (1) decrease in ER; (2) movement of the optimum NXP towards the inlet of the constant mixing chamber as demonstrated by Zhu *et al.* [11]. A decrease of 3.59% in ER for an increase of 1 °C in the primary temperature is noted. Moreover, a movement of 1.33 mm by the optimum NXP towards the inlet of the constant mixing chamber is observed. Figure 9 shows the pressure distribution on the ejector wall at three optimum NXPs for conditions C1, C2, and C3. From this figure, it is noted that the choking positions possess minimal pressures and exist in the constant mixing chamber, which is also demonstrated in [24]. Furthermore, the normal shock waves from the end of the constant mixing chamber appear to be the reason for the change in the supersonic flow to a subsonic flow [27,28].

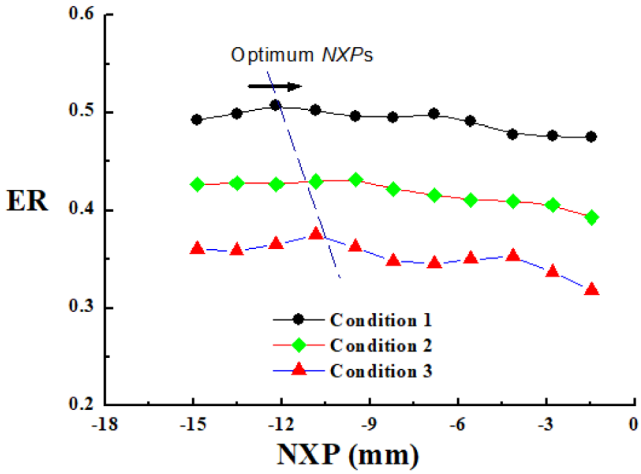

Figure 8. CFD distributions of entrainment ratios for three primary temperatures C1, C2, and C3.

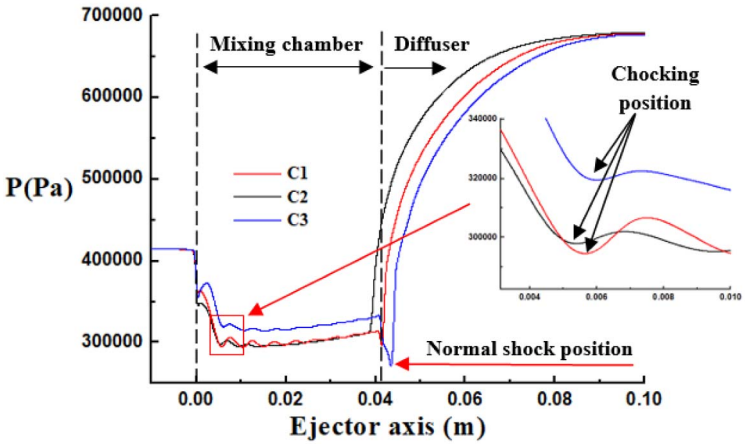

Figure 9. Pressure distributions on the ejector wall for three optimum NXPs for conditions C1, C2, and C3.

4.2.2. *Secondary temperature*

Figure 10 shows distributions of entrainment ratios at critical temperatures for three secondary temperatures (10, 7, and 5 °C), where the primary temperature is fixed at 89.15 °C. These conditions are represented by C3, C6, and C7 (Table 4b), respectively. It is reported that an increase in the secondary temperature produces two effects: (1) increase in ER; (2) recoil of the optimal NXP to the inlet of the mixing chamber. An increase of 5.52% in the entrainment ratio is provided by a rise of 1 °C in the secondary temperature and a movement of 1.27 mm by the optimum NXP to the inlet of the mixing chamber. The characteristics illustrated in Figures 8 and 10 can be explained by applying (3). An increase in the primary temperature causes a rise in the primary mass flow rate and keeps the secondary mass flow rate constant. Thus, ER decreases as shown in Figure 8. However, a rise in the secondary temperature involves an increase in the secondary

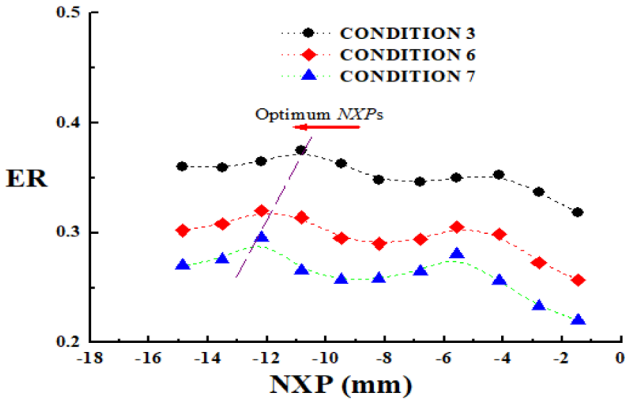

Figure 10. CFD distributions of entrainment ratios for three conditions C3, C6, and C7.

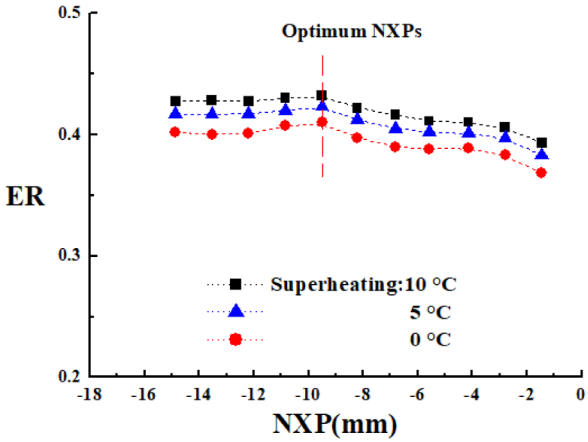

Figure 11. CFD distributions of entrainment ratios for three superheating temperatures 0, 5, and 10 °C for C2.

mass flow rate and keeps the primary mass flow rate constant. Thus ER increases as depicted in Figure 10.

4.2.3. *Superheating temperature*

Figure 11 presents the profiles of the entrainment ratio for three superheating temperatures (0, 5, and 10 °C) for fixed primary and secondary temperatures (84.39 and 10 °C, respectively). It is observed that ER increases with rise in the superheating temperature, but the optimal NXP remains fixed. Furthermore, an increase of 1 °C in the superheating temperature involves an increase of 0.97% in ER. Thus, ER benefits from the superheating of the fluid because the gas R134a is a wet fluid. Therefore, from Figures 8, 10, and 11, it is concluded that an increase of 1 °C in the secondary temperature provides a better increment in entrainment ratio than those provided by the primary and superheating temperatures. Table 8 presents the values of relative optimum δ and ejector enhancement for all the conditions tested and shown in Figures 8, 10, and 11. It is revealed that the CFD results of this work are different from the values cited in Table 1 particularly from the recommendations of ESDU [8].

Table 8. A summary of all optimum NXPs

Operating condition (°C) + Superheating temperature	C1 + 10	C2 + 10	C3 + 10	C3 + 10	C6 + 10	C7 + 10	C2 + 10	C2 + 5	C2 + 0
Optimum NXP (mm)	−12.19	−10.85	−10.85	−10.85	−12.19	−12.19	−9.50	−9.50	−9.50
δ	2.53	2.26	2.26	2.26	2.53	2.53	1.98	1.98	1.98
ER (CFD)	0.510	0.432	0.378	0.378	0.375	0.320	0.432	0.425	0.410
Enhancement of ER (%)	3.24	8.54	11.50	11.50	26.26	17.22	8.54	6.78	3.02

$$\delta = \left|\frac{\text{optimum NXP}}{D_{\text{Throat}}}\right| \qquad \text{Enhancement (\%)} = \left(\frac{\text{ER}_{\text{CFD}} - \text{ER}_{\text{EXP}}}{\text{ER}_{\text{EXP}}}\right) \cdot 100$$

5. Conclusion

This paper presents a CFD model for studying the performance of the supersonic ejector of a refrigeration system using R134 as the working fluid. The geometrical domain chosen is assumed to be two-dimensional and axisymmetric. The Navier–Stokes equations are discretized by the finite volume method of the commercial code Fluent. A combination of the REFPROP 7.0 database state equation and the high-Reynolds version of the SST k–ω model is used in simulations. The computed values show that the numerical model is well adapted to performance calculations of the ejector for different operating conditions. It has been shown that the relative errors in terms of the entrainment ratio and critical temperature do not exceed 5.13% and 5.41%, respectively, compared to the experimental data. In addition, it is noted that the optimum nozzle position is highly dependent on operating conditions. It is demonstrated that the entrainment ratio is improved when the primary temperature decreases and the optimum NXP moves to the constant mixing section. Furthermore, the entrainment ratio is improved when the secondary temperature rises and the optimum NXP moves to the constant mixing section. The enhancement of the superheating temperature improves slightly the entrainment but maintains the optimum NXP at a fixed position. It is also shown that an increase of 1 °C in the secondary temperature provides a better increment in the entrainment ratio (5.52%) than those provided by the primary and superheating temperatures (3.59% and 0.97%, respectively). Finally, all the computed values of the relative optimum NXPs from this study are different from the aforementioned reference values. The authors conclude that for designing an ejector with high entrainment performance in the on-design zone, the optimum NXP should be carefully selected for different operating conditions.

Nomenclature

		Unit
h	local enthalpy	(J)
E	total energy	(J)
Er	relative error	(-)
Ma	Mach number	(-)
P	static pressure	(Pa)
T	temperature	(K)
u	velocity	(m/s)
x	axial coordinate	(m)
y	transversal coordinate	(m)
$\dot{m}$	mass flow rate	(kg/s)
k	turbulence kinetic energy	(J)
ω	specific dissipation rate	(s^{-1})

Abbreviations

ER	entrainment ratio	(-)
NXP	nozzle exit position	(m)
COP	coefficient of performance	(-)

Greek letters

ρ	density	(kg/m^3)
μ	dynamic viscosity	(Ns/m^2)
τ	stress tensor	(N/m^2)

Subscripts

i, j, k	space components
eff	effective
CR	critical
DIF	diffuser
EV	evaporator
BO	boiler
CO	condenser
COM	compression
P	primary
S	secondary
DIS	discharge

References

[1] Z. Aidoun, K. Ameur, M. Falsafioon, M. Badache, "Current advances in ejector modeling, experimentation and applications for refrigeration and heat pumps. Part 1: single-phase ejectors", *Inventions* **4** (2019), no. 15, p. 1-73.

[2] C. Metin, O. Gök, A. U. Atmaca, A. Erek, "Numerical investigation of the flow structures inside mixing section of the ejector", *Energy* **166** (2019), p. 1216-1228.

[3] G. Besagni, R. Mereu, F. Inzoli, "Ejector refrigeration: a comprehensive review renewable and sustainable", *Energy Rev.* **53** (2016), p. 373-407.

[4] Y. Han, L. Guo, X. Wang, A. C. Y. Yuen, C. Li, R. Cao, H. Liu, T. B. Y. Chen, J. Tu, G. H. Yeoh, "A steam ejector refrigeration system powered by engine combustion waste heat: Part 2. Understanding the nature of the shock wave structure: Part 2. Characterization of the internal flow structure", *Appl. Sci.* **9** (2019), no. 4435, p. 1-16.

[5] W. Fu, Z. Liu, Y. Li, H. Wu, Y. Tang, "Numerical study for the influences of primary steam nozzle distance and mixing chamber throat diameter on steam ejector performance", *Int. Therm. Sci.* **132** (2018), p. 509-516.

[6] A. S. Ramesh, S. J. Sekhar, "Analytical and numerical studies of a steam ejector on the effect of nozzle exit position and suction chamber angle to fluid flow and system performance", *J. Appl. Fluid Mech.* **10** (2017), no. 1, p. 369-378.

[7] M. Falsafioon, Z. Aidoun, K. Ameur, "Numerical investigation on the effects of internal flow structure on ejector performance", *J. Appl. Fluid Mech.* **12** (2019), no. 6, p. 2003-2015.

[8] ESDU, "Ejector and jet pump", data item 86030, ESDU International Ltd, London, UK, 1985.

[9] B. Rifat, S. A. Omer, "CFD modelling and experimental investigation of an ejector refrigeration system using methanol as the working fluid", *Int. J. Energy Res.* **25** (2001), p. 115-128.

[10] I. W. Eames, A. E. Ablwaifa, V. Petrenko, "Results of an experimental study of an advanced jet-pump refrigerator operating with R245fa", *Appl. Therm. Eng.* **27** (2007), p. 2833-2840.

[11] W. Zhu, W. Cai, C. Wen, Y. Li, "Numerical investigation of geometry parameters for design of high-performance ejectors", *Appl. Therm. Eng.* **29** (2009), p. 898-905.

[12] J. Yan, W. Cai, Y. Li, "Geometry parameters effect for air-cooled ejector cooling systems with R134a refrigerant", *Renew. Energy* **46** (2012), p. 155-163.

[13] C. Lin, W. Cai, Y. Li, J. Yan, Y. Hu, K. Giridharan, "Numerical investigation of geometry parameters for pressure recovery of an adjustable ejector in multi-evaporator refrigeration system", *Appl. Therm. Eng.* **61** (2013), p. 649-656.

[14] V. V. Nguyen, S. Varga, J. Soares, V. Dvorak, A. C. Oliveira, "Applying a variable geometry ejector in a solar ejector refrigeration system", *Int. J. Refrig.* **113** (2020), p. 187-195.

[15] J. Dong, H. B. Ma, "Study of optimum Nozzle Exit Position (NXP) in a steam ejector refrigeration system", *Am. Inst. Phys. Conf. Ser.* **1547** (2013), p. 115-123.

[16] V. Kumar, P. M. V. Subbarao, G. Singha, "Effect of nozzle exit position (NXP) on variable area mixing ejector", *SN Appl. Sci.* **1** (2019), no. 11, article no. 1473.

[17] P. R. Pereira, S. Varga, A. C. Oliveira, J. Soares, "Development and performance of an advanced ejector cooling system for a sustainable built environment", *Front. Mech. Eng.* **1** (2015), no. 7, p. 1-12.

[18] A. S. Ramesh, S. J. Sekhar, "Experimental and numerical investigations on the effect of suction chamber angle and nozzle exit position of a steam-jet ejector", *Energy* **164** (2018), p. 1097-1113.

[19] J. García del Valle, J. J. Saiz, R. F. Castro, A. J. San Jose, "An experimental investigation of a R134a ejector refrigeration system", *Int. J. Refrig.* **45** (2014), p. 105-113.

[20] Y. Bartosiewicz, Z. Aidoun, P. Desevaux, Y. Mercadier, "CFD experiments integration in the evaluation of six turbulence models for supersonic ejector modeling", in *Conference Proc., Integrating CFD and Experiments*, 2003, Glasgow, UK.

[21] J. Gagan, K. Smierciew, D. Butrymowicz, J. Karwacki, "Comparative study of turbulence models in application to gas ejectors", *Int. J. Therm. Sci.* **78** (2014), p. 9-15.

[22] A. Inc., "ANSYS FLUENT, Theory Guide Release 14.5", 2012.

[23] N. Sharifi, M. Boroomand, "An investigation of thermo-compressor design by analysis and experiment: Part 1. Validation of the numerical method", *Energy Convers. Manage.* **69** (2013), p. 217-227.

[24] Y. Han, X. Wang, H. Sun, G. Zhang, L. Guo, J. Tu, "CFD simulation on the boundary layer separation in the steam ejector and its influence on the pumping performance", *Energy* **167** (2019), p. 469-483.

[25] G. Besagni, F. Inzoli, "Computational fluid-dynamics modeling of supersonic ejectors: screening of turbulence modeling approaches", *Appl. Therm. Eng.* **117** (2017), p. 122-144.

[26] R. Tillner-Roth, H. D. Baehr, "An international standard formulation for the thermodynamic properties of 1,1,1,2-tetrafluoroethane (HFC-134a) for temperatures from 170 K to 455 K and Pressures up to 70 MPa", *J. Phys. Chem. Ref. Data* **23** (1994), no. 5, p. 657-729.

[27] Y. A. Cengel, J. M. Cimbala, *Fluid Mechanics: Fundamentals and Applications, Introduction to Computational Fluid Dynamics*, McGraw-Hill, New York, USA, 2006.

[28] K. Matsuo, Y. Miyazato, H. D. Kim, "Shock train and pseudo-shock phenomena in internal gas flows", *Prog. Aerosp. Sci.* **35** (1999), p. 33-100.

[29] F. Riaz, P. S. Lee, S. K. Chou, "Thermal modelling and optimization of low-grade waste heat driven ejector refrigeration system incorporating a direct ejector model", *Appl. Therm. Eng.* **167** (2020), article no. 114710.